



Anomalous Nernst effect in the ceramic and thin film samples of $\text{La}_{0.7}\text{Sr}_{0.3}\text{CoO}_3$ perovskiteM. Soroka ^{1,2,3}, K. Knížek ^{1,*}, Z. Jiráček ¹, P. Levinský ¹, M. Jarošová ¹, J. Buršík ³ and J. Hejtmánek ¹¹*Institute of Physics of the Czech Academy of Sciences, 162 00 Prague 6, Czech Republic*²*Charles University, Faculty of Science, 128 43 Prague 2, Czech Republic*³*Institute of Inorganic Chemistry of the Czech Academy of Sciences, 250 68 Řež, Czech Republic*

(Received 9 November 2020; accepted 16 February 2021; published 1 March 2021)

We report the anomalous Nernst effect (ANE) in large-grain ceramics, nanogranular ceramics, and nanogranular thin films of $\text{La}_{0.7}\text{Sr}_{0.3}\text{CoO}_3$, measured over the temperature range 5–300 K. The study is complemented with thermopower, resistivity, and magnetic measurements. The temperature-dependent ANE below the Curie temperature T_C (240–250 K) is analyzed with the help of longitudinal resistivity and Seebeck using a previously proposed formula derived by a combination of Onsager reciprocity, the Mott formula, and the relation between transverse and longitudinal resistivity, $\rho_{xy} \propto \rho_{xx}^n$. We observe a characteristic exponent $n \sim 0.4$ in agreement with the universal scaling for the bad-metal-type conduction regime. The nanogranular samples are characterized by higher resistivity, lower saturated magnetization, and a higher coercive field compared to large-grain ceramics. On the other hand, the magnitude of the ANE is independent of grain size. This observation likely insinuates that the characteristic length scale characterizing the ANE in $\text{La}_{0.7}\text{Sr}_{0.3}\text{CoO}_3$ is below the grain size of nanogranular samples ~ 40 nm. Therefore, the ANE associated with the bad-metal regime is independent of barriers associated with grain surface, which are responsible for activated resistivity and lowered magnetization due to a magnetically “dead” layer. The observation that the advantage of the higher coercive field of nanogranular samples is not deteriorated by a lower ANE is important for possible applications in zero magnetic field.

DOI: [10.1103/PhysRevMaterials.5.035401](https://doi.org/10.1103/PhysRevMaterials.5.035401)**I. INTRODUCTION**

The $\text{La}_{1-x}\text{Sr}_x\text{CoO}_3$ solid solution is a member of the perovskite group of materials based on transition-metal oxides. Its fundamental characteristics were thoroughly investigated and were described by a rich phase diagram of structural, electronic, and magnetic properties [1–4]. The series $\text{La}_{1-x}\text{Sr}_x\text{CoO}_3$ exists for the whole solid solution range ($x = 0$ –1). The crystal structure is rhombohedral $R\bar{3}c$ for $x = 0$, and with increasing x the symmetry changes around $x \sim 0.5$ to cubic $Pm\bar{3}m$ [5–7]. The ground state of LaCoO_3 ($x = 0$) is diamagnetic with Co^{3+} at a low spin state ($t_{2g}^6 e_g^0$) and with increasing temperature is changed to paramagnetic with Co^{3+} successively at a mixture of a low and a high spin state ($t_{2g}^4 e_g^2$) and then at an intermediate spin state ($t_{2g}^5 e_g^1$) [8], although a definitive agreement on the character of high-temperature spin states has not yet been reached. Ferromagnetic (FM) order occurs above $x \sim 0.17$ with mixed valence $\text{Co}^{3+}/\text{Co}^{4+}$ ions in an intermediate spin state ($t_{2g}^5 e_g^1/t_{2g}^4 e_g^1$) due to the double exchange interactions between $\text{Co}^{3+}/\text{Co}^{4+}$ ions. Critical temperature T_C increases with x up to 230 K for $x = 0.3$, 250 K for $x = 0.5$, and 280 K for $x = 1$. Coherently the saturation magnetization increases with x within the range 0.2–0.5, in accordance with the intermediate spin state for both Co^{3+} ($S = 1$) and Co^{4+} ($S = 1.5$). However, the experimentally

observed magnetic moments are lower than the expected spin-only moment, namely for $x = 0.3$ the experimental moment 1.4–1.6 μ_B is reduced significantly compared to the theoretical moment 2.3 μ_B inferred from the simple ionic model [1–3]. The band-structure calculations have suggested that the hole doping in $\text{La}_{1-x}\text{Sr}_x\text{CoO}_3$ reduces the ionic character of the Co-O bond, enhances the hybridization between Co and O, and significantly renormalizes the magnetic moments of Co^{3+} and Co^{4+} [9].

Similar to magnetism, the transport properties depend on the doping level as well. Within the range $0 \leq x \lesssim 0.2$, the character of electrical resistivity is semiconducting at lower temperatures, and it exhibits a metal-insulator transition (MIT) at higher temperatures. Phases with $x \gtrsim 0.3$ exhibit a metallic type of resistivity over the whole temperature range. The Seebeck coefficient is high and positive for low x and is decreasing with increasing x approaching small “metalliclike” values above room temperature (RT) for $x > 0.2$. Moreover, at low temperatures the Seebeck coefficient becomes negative for $x \gtrsim 0.25$ [1,10].

In addition to its fundamental properties, the $\text{La}_{1-x}\text{Sr}_x\text{CoO}_3$ series offers many applications, e.g., as electrodes in solid oxide fuel, catalysts for the electrolysis of water, or sensors of chemical substances [11–15]. As one of the important prospects, it is considered as an alternative thermoelectric material for special uses [16–19]. Namely, it can be noted that the use of the presently most efficient materials for direct conversion of thermal energy to electric energy, such as Te alloys (Bi_2Te_3 , PbTe , and GeTe), doped skutterudites ($\text{Co}_4\text{Sb}_{12}$), or half-Heusler alloys, might be

* Author to whom all correspondence should be addressed: knizek@fzu.cz

restricted by several factors: (i) the potential negative environmental impact (e.g., in the case of Bi and Sb), (ii) the increasing price and low abundance of constituting elements (Ge, Hf, and Te), and (iii) the low temperature of melting and decomposition or oxidation in air at elevated temperatures. In contrast, the transition-metal oxides are generally cheap, environmentally friendly, and naturally stable at high temperatures.

Thermoelectric applications may also utilize significant transverse thermoelectric properties, namely the anomalous Nernst effect, which is observed in $\text{La}_{1-x}\text{Sr}_x\text{CoO}_3$ within the range of x with ferromagnetic order and metallic-type conductivity [20,21]. The transverse transport refers to the situation when two external fields, arranged along two perpendicular axes of the sample, induce charge/entropy density flows along the third remaining axis of the sample. For the Nernst effect, one of these stimulating fields is the thermal gradient ∇T and the other one is the orthogonally oriented magnetic field B . The transverse transport is generally revealed as the Nernst voltage V_N due to the accumulation of positive and negative charges on opposite sides of the sample in the direction of the third axis perpendicular to both ∇T and B .

Since the characteristic carrier mean free path and scattering mechanisms play an important role in the above-mentioned thermal and magnetothermal effects, we have focused on a comparison of the transverse thermoelectric effect (Nernst effect) measured on different bulk and nanostructured samples, in a form of ceramics and thin films, of $\text{La}_{0.7}\text{Sr}_{0.3}\text{CoO}_3$ ($x = 0.3$). All studied materials possess ferromagnetic order just below room temperature and metallic-type conductivity.

II. EXPERIMENT

Lanthanum strontium cobalt oxide $\text{La}_{0.7}\text{Sr}_{0.3}\text{CoO}_3$ thin films were deposited on the (h 00)-oriented SrTiO_3 (STO) single crystal (purchased from Crystal GmbH) by the chemical solution deposition (CSD) technique. 2-ethylhexanoates $[\text{CH}_3(\text{CH}_2)_3\text{CH}(\text{C}_2\text{H}_5)\text{COO}]_n\text{Me}$ ($n = 2$ for $\text{Me} = \text{Sr}, \text{Co}$; $n = 3$ for $\text{Me} = \text{La}$, ABCR, Germany) were used as metal precursors. Stoichiometric amounts of metal precursors and 2,2-diethanolamine (DEA) were dissolved in isobutanol. DEA was used as a modifier to slow down the reactivity and moisture sensitivity of metal precursors. The modifier to metal molar ratio was $n(\text{DEA})/n(\text{Me}) = 1$, and the overall metal concentration in deposition solution was $c(\text{La}^{3+} + \text{Sr}^{2+} + \text{Co}^{3+}) = 0.32 \text{ mol/L}$. Deposition solution was then mixed and heated overnight at 80°C to accomplish homogenization. All reactions and handling were done under a nitrogen atmosphere to prevent reaction with air humidity. The STO substrate was ultrasonically cleaned in an isopropanol bath to eliminate any surface contaminants, and then rinsed with deionized water. Prior to the deposition, substrates were treated with plasma (Zepto Plasma cleaner, Diener Electronic, Germany).

Using the spin-coating technique (spin coater RC8 Gyrset by KarlSuss), deposition solution was dropped onto the substrate and spun at 3000 rpm for 30 s. After the deposition step, the thin film was dried at 110°C for several minutes and pyrolyzed at 250°C for 5 min. Crystallization annealing

was done at 900°C for 10 min in a conventional tube furnace under O_2 flow. The deposition-crystallization step was repeated several times to obtain the target film thickness (0.30, 0.85, and $1.32 \mu\text{m}$). Then, final crystallization annealing was done at 900°C for 6 h in oxygen. Simultaneously with samples on STO, thin films on Si wafers were prepared under the same deposition conditions. These samples served for evaluation of film thicknesses by stylus apparatus (AlphaStep IQ, KLA Tencor).

A separate portion of deposition solution was transformed into powder samples by drying, pyrolysis, and crystallization annealing under identical conditions and served for chemical analysis by x-ray fluorescence (XRF, Rigaku NEX CG energy dispersive fluorescence spectrometer with an Rh 50 W x-ray source). This powder was then isostatically pressed and sintered at 900°C (ceramic nano) and 1100°C (ceramic bulk) in O_2 atmosphere to produce a ceramic sample for reference measurements. The ceramic bulk was subsequently annealed at 900°C under O_2 flow to ensure comparable oxygen stoichiometry with the ceramic nano sample. The stoichiometry of thin films was checked by electron microprobe analysis (EMPA, Jeol JXA-8230). Cross-section scanning electron microscopy (SEM) (FEIXX) analysis was used for a precise thickness determination. Atomic force microscopy (AFM, Bruker Dimension Icon) analysis in ScanAsyst mode was used to evaluate thin film surface topography.

The low-temperature (2–310 K) measurements of resistivity, thermopower, and thermal conductivity were performed using the four-probe method thermal transport option (TTO) of the Physical Property Measurement System (PPMS, Quantum Design) by using a specimen of length 8 mm and cross section $2 \times 2 \text{ mm}^2$. The Nernst effect was measured using a home-made apparatus employing the standard setup in which the directions of magnetic field, thermal gradient ∇T_x , and resulting electric field E_y are mutually perpendicular. The thickness of the measured ceramic samples in the direction of the temperature gradient was $L_x = 2 \text{ mm}$, in the direction of the magnetic field it was $L_z = 2 \text{ mm}$, and the electric contact distance was $L_y = 4 \text{ mm}$. In the case of the thin films, the temperature gradient ∇T_x was perpendicular to the film surface, and the dimensions L_y and L_z were the same. The small voltage signal V_y was measured using a Keithley 2182A nanovoltmeter, and the temperature difference ΔT_x was detected by differential thermocouples at the hot and cold sides of the samples. The Nernst signal S_{xy} was calculated according to the formula

$$S_{xy} = \frac{E_y}{\nabla T_x} = \frac{V_y}{L_y} \frac{L_x}{\Delta T_x} \quad (\mu\text{V/K}). \quad (1)$$

The magnetic response of the samples was measured within the temperature range 10–280 K using a superconducting quantum interference device (SQUID) magnetometer (MPMS, Quantum Design). The dimensions and orientation toward the magnetic field of the thin films were the same as in the Nernst effect measurements. The magnetization loops were measured by starting and ending at the maximum positive field (up to 40 kOe at low temperatures and up to 20 kOe at high temperatures), and the temperature was changing while the field was at the maximum positive value. The phase composition, the mean size of the crystallites, and the

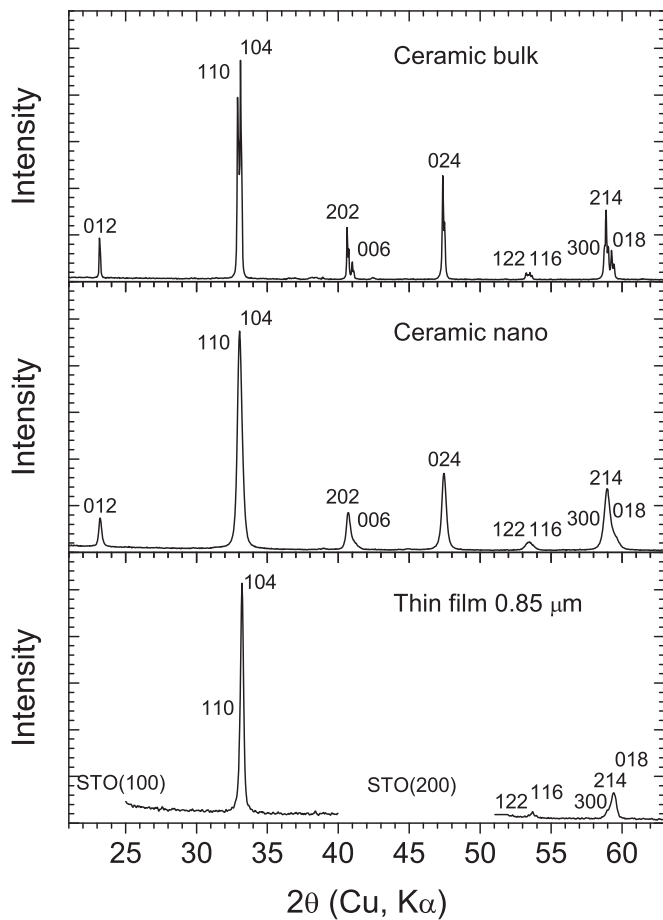


FIG. 1. X-ray diffraction patterns of the ceramic bulk and nano (40 nm) and thin film samples [reflections of SrTiO₃ substrate (STO) were skipped during measurement]. Reflections of the rhombohedral La_{0.7}Sr_{0.3}CoO₃ phase of $R\bar{3}c$ symmetry are indicated.

structural parameters of the products were analyzed by x-ray diffraction (XRD). The XRD patterns were acquired on a powder x-ray Bruker D8 Advance diffractometer with Cu $K\alpha$ radiation, and they were analyzed via the Rietveld method using the FULLPROF program [22]. The Thompson-Cox-Hastings pseudo-Voigt profile was applied for the profile analysis to resolve the strain and size contributions. The instrumental broadening was determined by the measurement of a strain-free LaB₆ standard. The microstructure of ceramic samples was analyzed by scanning electron microscopy (HR-SEM FEI NanoSEM 450). SEM analysis of thin films in a cross-section view served also for determination of film thickness.

III. RESULTS AND DISCUSSION

A. X-ray diffraction and SEM analysis

The x-ray diffraction confirmed a single perovskite phase for the ceramic and thin films samples (see Fig. 1). The analysis of the peak width showed an average size of the grains (crystallites) of ~ 40 nm for the sample annealed at 900 °C (further denoted as ceramic nano), whereas the sample annealed at 1100 °C (ceramic bulk) showed no broadening of the peaks compared to instrumental broadening. In the case of

thin films, x-ray diffraction also revealed the polycrystalline character of the samples with a low degree of preferred orientation in the c -direction quantified by the relative enhancement of the reflection ratio $(00l) : (hk0) \sim 10$ compared to the randomly oriented phase. The analysis of the peak width showed the average size of the grains (crystallites) was ~ 70 nm.

The thickness of the three La_{0.7}Sr_{0.3}CoO₃ films as determined from SEM cross-section images reach the values of 0.30, 0.85, and 1.32 μm ; see Figs. 2(a)–2(c). All of these thin films exhibited a generally similar porous microstructure consisting of grains with round shape morphology. The mean particle size was found to be ~ 82 nm [see Fig. 2(d)], which is close to the value obtained from the XRD pattern analysis. Figure 3 shows the microstructure of La_{0.7}Sr_{0.3}CoO₃ ceramic annealed at 900 °C [Figs. 3(c) and 3(d)] and 1100 °C [Figs. 3(a) and 3(b)]. It can be seen that the microstructure of ceramic changes with annealing temperature. Whereas the grain morphology of the sample annealed at 900 °C [Fig. 3(d)] is very similar to thin films, a higher annealing temperature leads to particle size growth and a change in their shape. We can see that a porous ceramic body composed of round-shaped particles (with an average particle size of ~ 43 nm) formed at 900 °C is transformed into material composed of more densely packed angular particles at higher annealing temperatures (with an average particle size of ~ 760 nm).

B. Magnetic properties

Magnetization curves at selected temperatures for ceramic bulk, ceramic nano, and thin film samples are displayed in Fig. 4. The magnetic properties of all thin films studied (thickness 0.30, 0.85, and 1.32 μm) are similar (not shown). Figure 4 displays properties of 0.85 μm film as an example. The diamagnetic signal of SrTiO₃ substrate was measured separately and subtracted from the signal of the thin film sample. All samples are ferromagnetic at low temperature, and transition to a paramagnetic state takes place between 240 and 250 K.

A difference in the magnetic properties between the bulk and nanogranular ceramic samples can be clearly observed. In the case of bulk ceramics, the saturated magnetic moment at 10 K reaches a value $\sim 1.5 \mu_B$, which is in agreement with previous experiments [1–3]. The coercive field (H_c) is linearly increasing from T_C down to low temperature with the maximum value of 0.56 kOe at 10 K. The saturated magnetization of the nanogranular ceramic sample is much smaller with a maximum value of 0.75 μ_B at 10 K, i.e., about 50% compared to bulk ceramics. The coercive field is also increasing linearly with lowering temperature, but is much higher than in the case of bulk ceramics and rises to 4.2 kOe at 10 K. Finally, the magnetic properties of the thin films, close to that of the nanogranular ceramic sample, affirm the nanoscopic nature of thin films with a maximum coercive field of 3.8 kOe at 10 K. The saturated magnetization was determined as 1.05 μ_B , i.e., 70% compared to ceramic bulk.

Smaller magnetization of the ceramic nano and thin film samples can be largely explained by the presence of the magnetically dead layer on the grain surface, which was observed, e.g., in structurally similar nanogranular manganese perovskites [23–25] of a thickness about 1.5–2.5 nm. The magnetism in La_{1-x}Sr_xCoO₃ perovskites, similarly to Mn

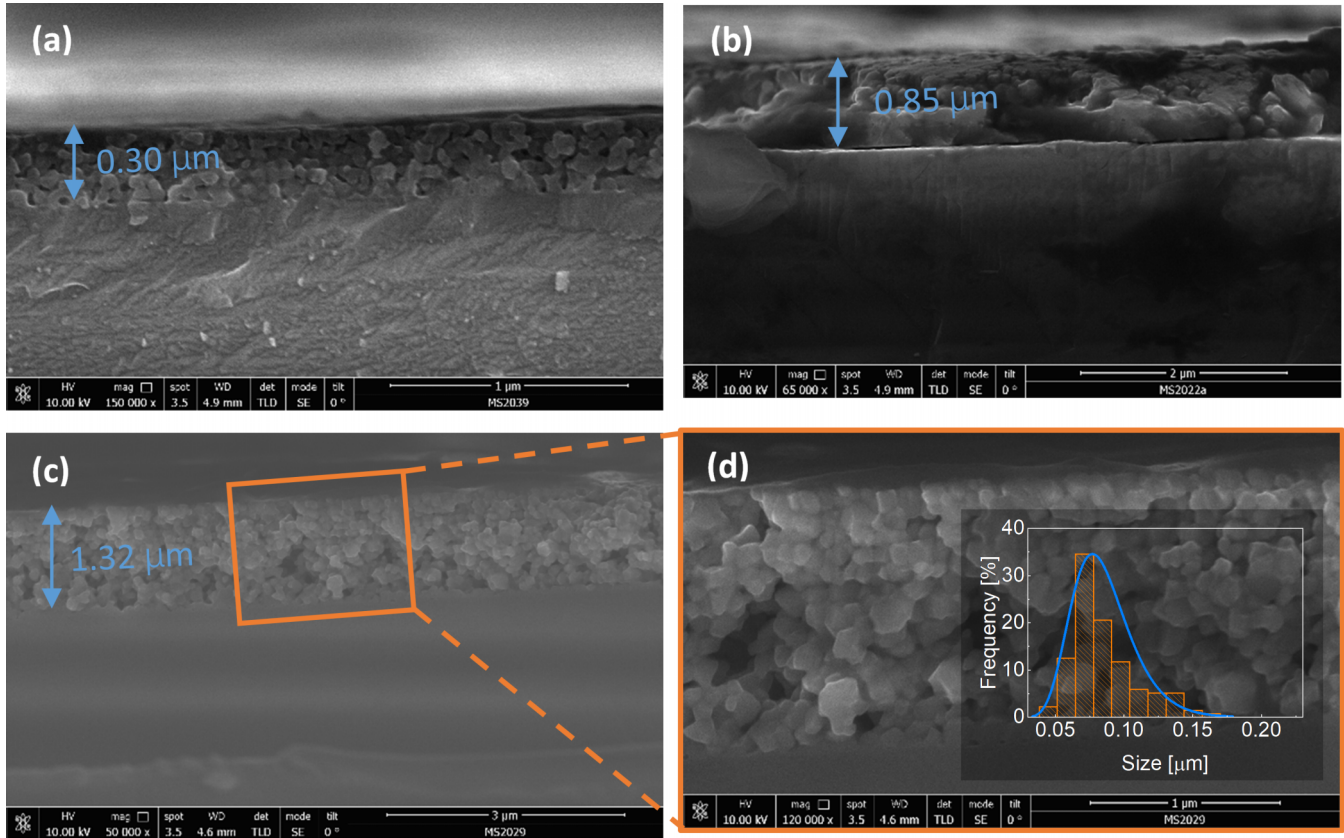


FIG. 2. (a)–(c) SEM images in cross-section view of the $\text{La}_{0.7}\text{Sr}_{0.3}\text{CoO}_3$ thin films with different thickness. (d) Detailed view of the thin film microstructure with inserted particle size histogram.

perovskites, is a result of the dominant FM double exchange mediated by itinerant e_g carriers. It can be anticipated that the mobility of e_g carriers, and thus the strength of the FM double exchange, is significantly restrained at the particle surface. In our case, the presence of, e.g., a 2 nm dead layer on the surface of ~ 40 nm grains of the ceramic nano sample would lower the saturated magnetization to $\sim 70\%$. For thin film with 70 nm grains, the same thickness of the dead layer would lower the saturated magnetization to 84%. Comparing with experimentally observed lowering of magnetization (50% and 70% for the two samples, respectively), we may conclude that the dead layer in Co perovskites is either twice as thick or there should be some other reason for the lowering magnetization, e.g., the partial structural and magnetic disorder.

We note that enhanced coercivity in ceramic samples of $\text{La}_{1-x}\text{Sr}_x\text{CoO}_3$ with decreasing grain size was also observed in [26]. The high coercive field of 9 kOe for a grain size of 26 nm was explained by a domain wall pinning on the grain boundaries. Similarly, the high coercivity up to 14.5 kOe, observed in cobaltite thin films with 40 nm thickness grown on SrTiO_3 substrates, was explained by strain-induced changes of crystal structure, and consequently by electronic structure changes, together with a possible contribution of enhanced domain wall pinning by the tensile strain [27]. Nevertheless, a high coercive field up to 9 kOe was also observed in thin films grown on $(\text{LaAlO}_3)_{0.3}(\text{Sr}_2\text{AlTaO}_6)_{0.7}$ (LSAT) substrates with minimal strain [28]. In our case, the enhanced coercivity observed in the ceramic nano sample and thin films is evidently

related to the size of the grains. Therefore, we consider the enhanced domain wall pinning on the grain boundaries as the most plausible explanation.

C. Longitudinal transport properties

Longitudinal electric and thermal transport properties, i.e., thermopower, electrical resistivity, and thermal conductivity, were measured for ceramic samples; see Fig. 5. The critical FM temperature T_C is manifested by an obvious anomaly at around 240–250 K in the temperature dependence of the Seebeck coefficient and electrical resistivity for both the bulk and nanogranular samples, whereas the course of the thermal conductivity does not exhibit any anomaly at T_C . The temperature dependence of the Seebeck coefficient for the ceramic bulk sample agrees with previous reports [1,26]. The linear part above T_C , which can be extrapolated to zero, is identified as diffusion thermopower typical for materials with intrinsic metallic resistivity. A significant negative additional contribution occurs just below T_C and can be assigned either to magnon or phonon drag [29,30]. Nonetheless, we interpreted it as magnon drag, the key argument being (i) the onset at the same temperature as a formation of the long-range ferromagnetic order, and (ii) the low thermal conductivity, which evidently disadvantages phonon drag due to the extremely short phonon mean free path. The diffusion thermopower is positive, reflecting the hole character of charge carriers, in contrast to the negative magnon drag contribution. We note

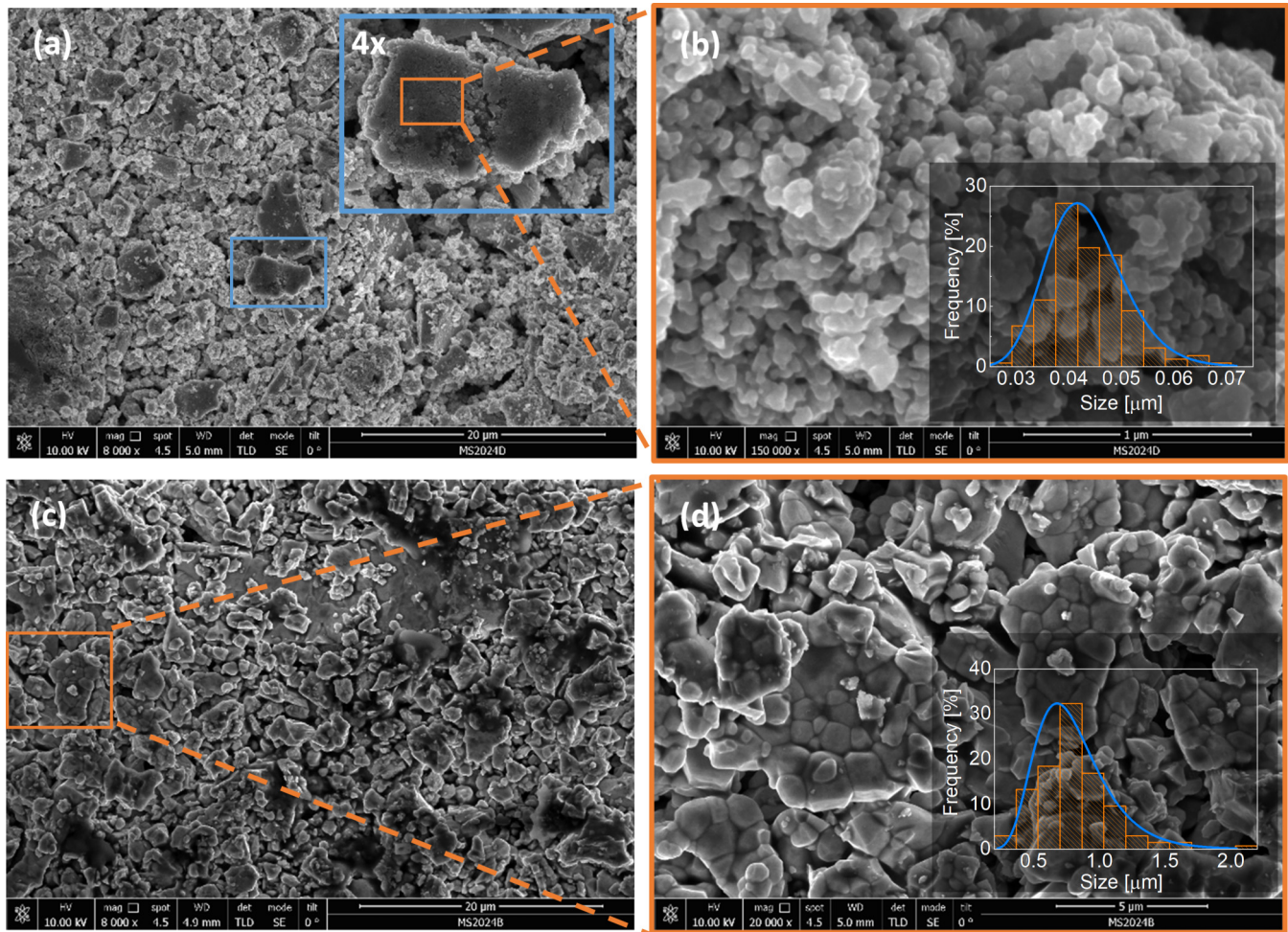


FIG. 3. SEM images of $\text{La}_{0.7}\text{Sr}_{0.3}\text{CoO}_3$ ceramic samples annealed at (a), (b) 900°C and (c), (d) 1100°C .

that the situation in which the magnon drag has the opposite sign to that of the diffusion thermopower occurs when the effect of magnon decay, characterized by the Gilbert damping parameter, prevails over the viscous hydrodynamic magnon drag, which, contrary to that, lifts up the diffusing thermopower keeping the same sign [29,30]. The thermopower of the ceramic nano sample displays the same behavior, i.e., positive diffusion thermopower and negative magnon drag contribution below T_C . The magnon drag contribution is, however, smaller due to the lower degree of ordering of the FM structure manifested by the lower saturated magnetization. The high-temperature part is shifted by an approximately constant value $9 \mu\text{V}/\text{K}$ to positive values. A similar shift to positive values with decreasing grain size was also observed in [26].

Let us note that synthesis conditions of the ceramic nanosample, i.e., a lower synthesis temperature of 900°C compared to 1100°C for the ceramic bulk sample, could also produce higher oxygen stoichiometry of the nano sample. Therefore, we have subsequently annealed the ceramic bulk sample at 900°C to level out the oxygen stoichiometry. Nevertheless, the influence of oxygen stoichiometry on the Seebeck coefficient could be excluded, since the higher oxygen content should have a similar effect to that of higher Sr doping, i.e., a higher ratio of Co^{4+} to Co^{3+} according to the formula

$\text{La}_{1-x}\text{Sr}_x\text{Co}_{1-x-2\delta}^{3+}\text{Co}_{x+2\delta}^{4+}\text{O}_{3+\delta}$, and with higher Sr content the Seebeck coefficient decreases to more negative values, i.e., it would be shifted in the opposite direction to that observed in our case [1,10].

The resistivity course of the ceramic bulk sample is of metallic type, i.e., increasing with increasing temperature. The temperature dependence below T_C could thus be interpreted as a sum of the residual resistivity due to the scattering on defects or impurities, the electron-electron scattering in $s-d$ orbitals of transition metals (described by an $R_{ee}T^2$ temperature dependence), and the electron-magnon scattering ($R_{em}T^{4.5}$) [31],

$$\rho = \rho_0 + R_{ee}T^2 + R_{em}T^{4.5}. \quad (2)$$

Actually, the fit of the data cannot distinguish between electron-phonon ($R_{ep}T^5$) and electron-magnon ($R_{em}T^{4.5}$) scattering, but we have considered the dominance of electron-magnon scattering since the Seebeck coefficient displays magnon drag rather than phonon drag. A small increment of the resistivity observed below ~ 30 K can be interpreted as a consequence of weak localization due to the structural or magnetic disorder [32]. The actually observed resistivity of $0.37 \text{ m}\Omega \text{ cm}$ at 30 K (at minimum resistivity) and $0.85 \text{ m}\Omega \text{ cm}$ at 250 K (at T_C) can be compared with analogous data from Ref. [20] acquired on single crystal, namely $0.05 \text{ m}\Omega \text{ cm}$ at

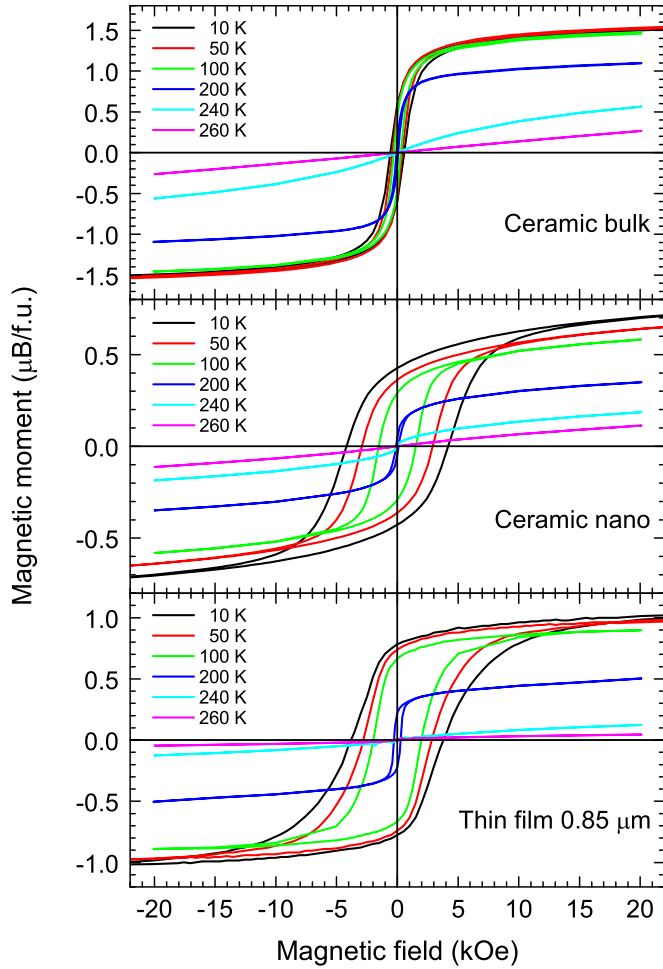


FIG. 4. Magnetization curves at selected temperature for ceramic bulk and nano samples and thin film with a thickness of 0.85 μm .

30 K and 0.19 $\text{m}\Omega\text{cm}$ at 250 K. The rather small resistivity difference between T_C and 30 K, $\Delta R \sim 0.48 \text{ m}\Omega\text{cm}$, compared to 0.14 $\text{m}\Omega\text{cm}$ in single crystal, confirms the good quality of our bulk ceramics.

As seen further in Fig. 5, the absolute value of resistivity of the ceramic nano sample at T_C (7.0 $\text{m}\Omega\text{cm}$) is about $8\times$ higher than the resistivity of the ceramic bulk sample. Below this temperature, the resistivity takes a decreasing trend, reaches a shallow minimum around 140 K, and then slowly increases up to 8.4 $\text{m}\Omega\text{cm}$ at 5 K. Such a temperature dependence can be interpreted in terms of a core-shell structure, where the grain boundaries of the ceramic nano sample display an “insulating” behavior while the core region of each grain exhibits metallic properties of the bulk. The transmission of charge carriers through the grain boundary barrier can be analyzed within the framework of a model in which the existence of a Coulomb gap E_C , superimposed to quantum tunneling between nano-sized grains, produces a significant blockade at temperatures below ~ 140 K.

Thermal conductivity of both samples reflects the situation in which the thermal conductivity of predominantly phononic origin increases with temperature due to increasing heat capacity while the mean free path of phonons remains roughly constant as a consequence of strong scattering due to the

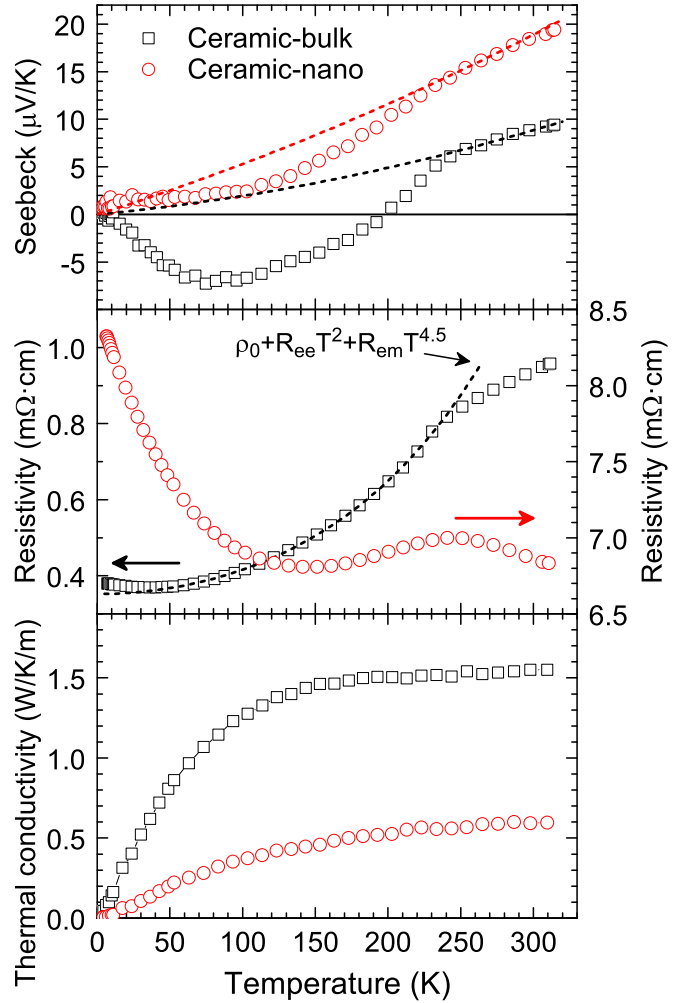


FIG. 5. Seebeck coefficient, resistivity, and thermal conductivity dependence on temperature for ceramic samples. The dashed lines in the Seebeck graph refer to estimated diffusion thermopower. The dashed line in the resistivity graph refers to the fit by Eq. (2).

mixed valence of $\text{Co}^{3+}/\text{Co}^{4+}$ ions, La-Sr substitution, and the ceramic nature of the samples. The significantly higher “ceramic” quality of the ceramic bulk sample is, however, corroborated by the thermal conductivity of the ceramic bulk sample, which saturates at $\sim 1.5 \text{ W/K/m}$, while the nanostructuring is responsible for about a three times smaller value observed in the ceramic nano sample.

D. Nernst effect

The dependence of the Nernst effect on the magnetic field for selected temperatures is displayed in Fig. 6 for ceramic bulk and nano samples and thin film with a thickness of 0.85 μm . The total signal of the Nernst effect (S_{xy}) is composed of the ordinary and anomalous contributions (S_{xy}^O and S_{xy}^A) according to the relation

$$S_{xy} = S_{xy}^O H + S_{xy}^A(M). \quad (3)$$

Whereas the ordinary Nernst effect is linearly proportional to the applied magnetic field (H), the anomalous Nernst effect

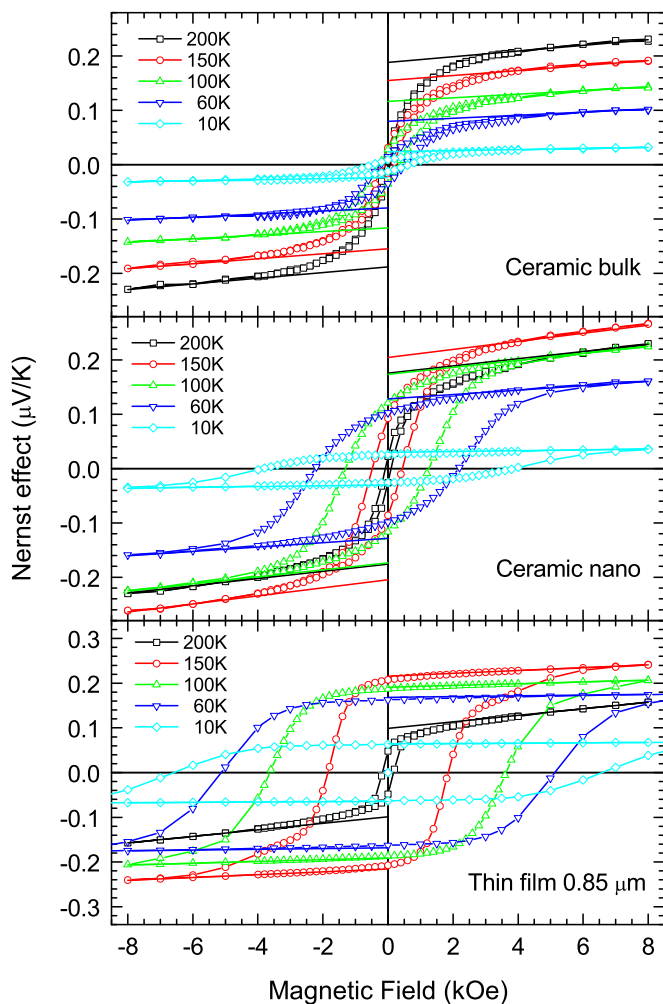


FIG. 6. Nernst effect curves at selected temperatures for ceramic bulk and nano samples, and thin film with a thickness of 0.85 μm.

(ANE) follows the field dependence of magnetization (M). The ordinary Nernst coefficient S_{xy}^O was extracted as the slope of the linear extrapolation of the high-field part of the hysteresis curves, and the constant part of the remaining curve was taken as the amplitude of ANE; see Fig. 7. Unfortunately, the Nernst coefficient S_{xy}^O cannot be determined unambiguously, because the slope of the linear fit includes also the increase of the ANE due to the increasing magnetization, since the magnetization is not yet saturated within the range of the measured field. Therefore, we have essentially focused on the analysis of the ANE.

The coercive fields of the ceramic samples determined from the Nernst effect are similar to coercive fields determined

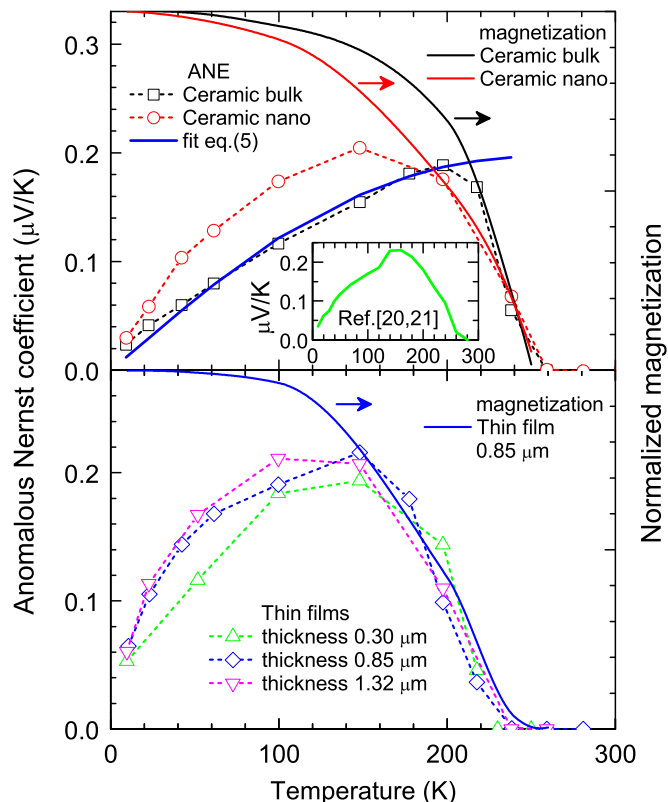


FIG. 7. Anomalous Nernst effect dependence on temperature for ceramic (upper) and thin film (lower) samples. Fit of ceramic bulk sample data with formula (5) and a comparison with magnetization is also displayed. The inset shows the data from Refs. [20,21].

from magnetization data, i.e., the ceramic nano sample shows a larger H_c than the ceramic bulk sample. The coercive fields of thin films determined from the Nernst effect are roughly the same for various film thicknesses and, surprisingly, are much larger than H_c from magnetization; see Table I. We can see that the coercive fields follow the trend given by the grain sizes, with the exception of H_c of thin films observed in the Nernst effect. A plausible explanation is that the Nernst effect largely reflects the properties of the upper parts of the spin-coated film, which differ from the deeper parts by essentially the smaller size of the crystallites and their intergrowth. A detailed analysis is provided in the Supplemental Material [33], where a comparison of hysteresis curves for the Nernst effect and magnetization is displayed in Fig. S1.

The dependences of the ANE on the temperature are displayed in Fig. 7. The ANE signal starts to increase just below T_C for all samples. It increases more steeply for the ceramic

TABLE I. Comparison of coercive fields determined at 10 K from magnetization and ANE data, and the grain sizes determined by XRD and SEM.

Sample	Coercive field H_c (kOe)		Average grain size (nm)	
	Magnetization	ANE	SEM	XRD
Ceramic bulk	0.56	0.56	760	>500
Thin film 0.85 μm	3.8	6.6	82	70
Ceramic nano	4.2	4.0	43	40

bulk sample and reaches a maximum around 200 K, whereas the increase below T_C for the ceramic nano sample is slower, and a maximum is reached around 150 K. This behavior is closely related to the increase of magnetization with temperature, which is also slower for the nano sample, as can be seen from the comparison of ANE with normalized magnetization extrapolated to zero field. Below the maximum, the ANE signal decreases toward zero. The temperature dependence of ANE of thin film samples is quite similar for all films, i.e., it does not significantly vary with the film thickness. The overall behavior of the temperature dependence of ANE of thin film samples resembles that of the ceramic nano sample.

The observation that the magnitude and temperature dependence of the ANE is similar for all samples is surprising considering that the longitudinal transport properties and saturated magnetizations, i.e., the properties that should significantly influence the magnitude of ANE, are significantly different for the ceramic bulk and nano samples. Namely, the ceramic bulk sample displays metallic conductivity, whereas the ceramic nano sample displays transition from metallic resistivity to the regime of Coulomb blockade at low temperature. The magnetization is significantly lower for samples with smaller grain sizes. In addition, our ANE data can be compared with data acquired on a single-crystal sample presented as electrical conductivity σ_{xx} in [20] and thermoelectric conductivity α_{xy} in [21] and recalculated for the sake of comparison by an approximate formula $S_{xy} = \alpha_{xy}/\sigma_{xx}$ (where $\sigma_{xx} \gg \sigma_{xy}$); see the inset in Fig. 7. We can see that the maximum of the single-crystal ANE is the same as that for our samples, and the temperature dependences are quite similar. In summary, the ANE characteristics are shown to be remarkably similar for $\text{La}_{0.7}\text{Sr}_{0.3}\text{CoO}_3$ samples with various morphologies, namely for single crystals, ceramic bulk, ceramic nano, and thin films. Nonetheless, for possible applications in zero magnetic field, the higher coercive field of ceramic nano samples and thin films is a clear advantage.

To analyze in more detail the temperature dependence of ANE, we have employed a formula proposed in [34,35], which relates the ANE (S_{xy}) with the longitudinal resistivity ρ_{xx} and Seebeck coefficient S_{xx} , and was derived from the following three principles: (i) The Onsager reciprocal relations that link together longitudinal and transverse transport coefficients [36]. (ii) The Mott formula that links together the longitudinal Seebeck coefficient S_{xx} and the energy derivative of the electrical conductivity σ_{xx} at the Fermi level E_F [37],

$$S_{xx} = \frac{\pi^2 k_B^2 T}{3e \sigma_{xx}} \left(\frac{\partial \sigma_{xx}}{\partial E} \right)_{E_F}, \quad (4)$$

where k_B is the Boltzmann constant and e is the charge of the carriers. In the presence of a magnetic field, the Mott relation similarly holds for the transverse transport coefficient S_{xy} in terms of σ_{xy} . (iii) The assumption that both the anomalous Nernst and anomalous Hall effects (AHE) originate from the same mechanisms, and, therefore, the models developed for AHE can be applied for ANE, too [34]. Regarding AHE, several models linking anomalous Hall resistivity ρ_{xy}^{AH} and longitudinal resistivity ρ_{xx} have been devised in the form $\rho_{xy}^{\text{AH}} \sim \lambda \rho_{xx}^n$, with n and λ as nondimensional exponent and prefactor [38]. The intrinsic models that only depend on

the ideal band structure and are independent of scattering include interband effect [39] and Berry phase [40,41] mechanisms. The models based on extrinsic mechanisms include skew-scattering [42] and side-jump [43]. The models can be distinguished by the exponent n in the above-mentioned power-law relation. The intrinsic and side-jump mechanisms can be modeled with exponent $n = 2$. In contrast, the skew-scattering mechanism predicts $n = 1$. In addition, the model for phases in the bad-metal conduction regime proposes $n \sim 0.4$ [21,44]. The resulting formula, which combines the three above-described principles and relates ANE (S_{xy}) with the longitudinal resistivity ρ_{xx} and the Seebeck coefficient S_{xx} , takes the following form [34,35]:

$$S_{xy} = \rho_{xx}^{(n-1)} \left[\frac{\pi^2 k_B^2}{3e} \lambda' T - (n-1) \lambda S_{xx} \right]. \quad (5)$$

This formula contains three fitting parameters, namely n and λ described above and λ' , which is the energy derivative of λ . Its validity has been tested for the intrinsic mechanism [34,45], the skew scattering mechanism [46], and also for the bad-metal conduction regime [35].

The fit using Eq. (5) for the ceramic bulk sample within the temperature range 10–200 K (well below T_C) is displayed in Fig. 7. The resulting fitting parameters are $n = 0.39$, $\lambda = 1.53 \times 10^{-3}$, and $\lambda' = 1.84 \times 10^{18}$. The exponent of the power law $n = 0.39$ corresponds to the bad-metal conduction regime that is predicted for materials with resistivity higher than $\sim 10^{-1} \text{ m}\Omega \text{ cm}$, which is evidently the case for the ceramic bulk sample. However, the same fit was not possible to apply for the ceramic nano sample, principally because the character of electric transport is strongly influenced by the tunneling through grain boundaries combined with the Coulomb blockade, resulting in certain localization seen over a wide low-temperature range.

IV. CONCLUSIONS

The anomalous Nernst effect, completed by measuring transport and magnetization properties, has been investigated in ceramic and thin film samples $\text{La}_{0.7}\text{Sr}_{0.3}\text{CoO}_3$. The magnitude of ANE is similar for all samples and resembles the data reported for a single crystal in [20,21]. Of special interest is also its temperature dependence below the Curie temperature ($T_C \sim 240\text{--}250 \text{ K}$). It is analyzed using the Mott formula and the relation between the transverse and longitudinal resistivity as proposed in [34,35]. The characteristic exponent $n \sim 0.4$ is determined in agreement with the universal scaling for the bad-metal type conduction regime.

Our finding that ANE is insensitive to sample forms and morphologies is surprising, considering that the longitudinal transport properties and magnetizations are significantly different for ceramic bulk and nano samples. Namely, the ceramic bulk sample displays metallic conductivity of standard temperature dependence whereas the related nanogranular sample exhibits a transition from metallic conduction to a thermally activated type at low temperature, and the saturated magnetization is almost twice as small. We thus conclude that the typical carrier-length scale characterizing transverse transport in $\text{La}_{0.7}\text{Sr}_{0.3}\text{CoO}_3$ is below the grain size $\sim 40 \text{ nm}$ of the studied nano samples, for which ANE does not reflect

the enhanced role of grain boundaries seen in resistivity and the Seebeck coefficient. On the other hand, the ANE naturally mimics a higher coercive field in nanostructured samples. The higher coercive field of nano samples while keeping favorable ANE characteristics is important for possible applications in zero magnetic field.

ACKNOWLEDGMENTS

This work was supported by Projects No. 19-06433S and No. 18-12761S of the Czech Science Foundation. We also

acknowledge the support by Operational Programme Research, Development and Education financed by European Structural and Investment Funds and the Czech Ministry of Education, Youth, and Sports (Project No. SOLID21-CZ.02.1.01/0.0/0.0/16_019/0000760), and by the Research Infrastructure NanoEnviCZ, supported by the Czech Ministry of Education, Youth, and Sports (LM2018124). The magnetic experiments were performed at Materials Growth & Measurement Laboratory (MGML) [47], which is supported within the program of Czech Ministry of Education, Youth, and Sports (Project No. LM2018096).

-
- [1] M. A. Señaris-Rodríguez and J. B. Goodenough, Magnetic and transport properties of the system $\text{La}_{1-x}\text{Sr}_x\text{CoO}_3$ ($0 < x \leq 0.5$), *J. Solid State Chem.* **118**, 323 (1995).
- [2] J. Wu and C. Leighton, Glassy ferromagnetism and magnetic phase separation in $\text{La}_{1-x}\text{Sr}_x\text{CoO}_3$, *Phys. Rev. B* **67**, 174408 (2003).
- [3] D. Samal and P. S. Anil Kumar, A critical re-examination and a revised phase diagram of $\text{La}_{1-x}\text{Sr}_x\text{CoO}_3$, *J. Phys.: Condens. Matter* **23**, 016001 (2011).
- [4] P. Bezdička, A. Wattiaux, J. C. Grenier, M. Pouchard, and P. Hagemuller, Preparation and characterization of fully stoichiometric SrCoO_3 by electrochemical oxidation, *Z. Anorg. Allg. Chem.* **619**, 7 (1993).
- [5] R. Caciuffo, D. Rinaldi, G. Barucca, J. Mira, J. Rivas, M. A. Señaris-Rodríguez, P. G. Radaelli, D. Fiorani, and J. B. Goodenough, Structural details and magnetic order of $\text{La}_{1-x}\text{Sr}_x\text{CoO}_3$ ($x \leq 0.3$), *Phys. Rev. B* **59**, 1068 (1999).
- [6] V. G. Sathe, A. V. Pimpale, V. Siruguri, and S. K. Paranjpe, Neutron diffraction studies of perovskite-type compounds $\text{La}_{1-x}\text{Sr}_x\text{CoO}_3$ ($x = 0.1, 0.2, 0.3, 0.4, 0.5$), *J. Phys.: Condens. Matter* **8**, 3889 (1996).
- [7] A. Mineshige, M. Inaba, T. Yao, Z. Ogumi, K. Kikuchi, and M. Kawase, Crystal structure and metal-insulator transition of $\text{La}_{1-x}\text{Sr}_x\text{CoO}_3$, *J. Solid State Chem.* **121**, 423 (1996).
- [8] K. Knížek, Z. Jiráček, J. Hejtmánek, P. Novák, and W. Ku, GGA+U calculations of correlated spin excitations in LaCoO_3 , *Phys. Rev. B* **79**, 014430 (2009).
- [9] P. Ravindran, H. Fjellvåg, A. Kjekshus, P. Blaha, K. Schwarz, and J. Luitz, Itinerant metamagnetism and possible spin transition in LaCoO_3 by temperature/hole doping, *J. Appl. Phys.* **91**, 291 (2002).
- [10] K. Iwasaki, T. Ito, T. Nagasaki, Y. Arita, M. Yoshino, and T. Matsui, Thermoelectric properties of polycrystalline $\text{La}_{1-x}\text{Sr}_x\text{CoO}_3$, *J. Solid State Chem.* **181**, 3145 (2008).
- [11] G. M. Rupp, A. K. Opitz, A. Nanning, A. Limbeck, and J. Fleig, Real-time impedance monitoring of oxygen reduction during surface modification of thin film cathodes, *Nat. Mater.* **16**, 640 (2017).
- [12] Y. Lu, C. Kreller, and S. B. Adler, Measurement and modeling of the impedance characteristics of porous $\text{La}_{1-x}\text{Sr}_x\text{CoO}_{3-\delta}$ electrodes, *J. Electrochem. Soc.* **156**, B513 (2009).
- [13] S. B. Adler, Mechanism and kinetics of oxygen reduction on porous $\text{La}_{1-x}\text{Sr}_x\text{CoO}_{3-\delta}$ electrodes, *Solid State Ion.* **111**, 125 (1998).
- [14] T. Mefford, X. Rong, A. M. Abakumov, W. G. Hardin, S. Dai, A. M. Kolpak, K. P. Johnston, and K. J. Stevenson, Water electrolysis on $\text{La}_{1-x}\text{Sr}_x\text{CoO}_{3-\delta}$ perovskite electrocatalysts, *Nat. Commun.* **7**, 11053 (2016).
- [15] H. Liu, Y. Guo, R. Xie, T. Peng, G. Ma, and Y. Tang, Novel acetone sensing performance of $\text{La}_{1-x}\text{Sr}_x\text{CoO}_3$ nanoparticles at room temperature, *Sens. Actuator B* **246**, 164 (2017).
- [16] A. J. Zhou, J. Zhu, and X. B. Zhao, Thermoelectric properties of perovskite oxides $\text{La}_{1-x}\text{Sr}_x\text{CoO}_3$ prepared by polymerized complex method, *J. Mater. Sci.* **43**, 1520 (2008).
- [17] Z. Viskadourakis, M. Pervolaraki, G. I. Athanasopoulos, and J. Giapintzakis, Thermoelectric properties of strained, lightly-doped $\text{La}_{1-x}\text{Sr}_x\text{CoO}_3$ thin films, *J. Appl. Phys.* **125**, 055102 (2019).
- [18] Z. Viskadourakis, G. I. Athanasopoulos, E. Kasotakis, and J. Giapintzakis, Effect of microstructure on the thermoelectric performance of $\text{La}_{1-x}\text{Sr}_x\text{CoO}_3$, *J. Solid State Chem.* **243**, 111 (2016).
- [19] M. A. Bousnina, R. Dujardin, L. Perriere, F. Giovannelli, G. Guegan, and F. Delorme, Synthesis, sintering, and thermoelectric properties of the solid solution $\text{La}_{1-x}\text{Sr}_x\text{CoO}_{3+d}$ ($0 \leq x \leq 1$), *J. Adv. Ceram.* **7**, 160 (2018).
- [20] Y. Onose and Y. Tokura, Doping dependence of the anomalous Hall effect in $\text{La}_{1-x}\text{Sr}_x\text{CoO}_3$, *Phys. Rev. B* **73**, 174421 (2006).
- [21] T. Miyasato, N. Abe, T. Fujii, A. Asamitsu, S. Onoda, Y. Onose, N. Nagaosa, and Y. Tokura, Crossover Behavior of the Anomalous Hall Effect and Anomalous Nernst Effect in Itinerant Ferromagnets, *Phys. Rev. Lett.* **99**, 086602 (2007).
- [22] J. Rodríguez-Carvajal, *Physica B* **192**, 55 (1993), <http://ill.eu/sites/fullprof> (ILL JRC, Version 5.60 – Jan2015).
- [23] T. Sarkar, A. K. Raychaudhuri, and S. M. Yusuf, Effect of size reduction on the ferromagnetism of the manganese $\text{La}_{1-x}\text{Ca}_x\text{MnO}_3$ ($x = 0.33$), *New J. Phys.* **12**, 123026 (2010).
- [24] D. Rybicki, M. Sikora, Cz. Kapusta, P. C. Riedi, Z. Jiráček, K. Knížek, M. Maryško, E. Pollert, and P. Veverka, A ^{55}Mn NMR study of the $\text{La}_{0.75}\text{Sr}_{0.25}\text{MnO}_3$ nanoparticles, *Phys. Status Solidi C* **3**, 155 (2006).
- [25] Z. Jiráček, M. Kačenka, O. Kaman, M. Maryško, N. M. Belozeroва, S. E. Kichanov, and D. P. Kozlenko, Role of surface on magnetic properties of $\text{La}_{1-x}\text{Sr}_x\text{MnO}_{3+d}$ nanocrystallites, *IEEE Trans. Magn.* **51**, 1000204 (2015).
- [26] O. J. Dura, P. Rogl, M. Falmbigl, G. Hilscher, and E. Bauer, Thermoelectric and magnetic properties of nanocrystalline $\text{La}_{0.7}\text{Sr}_{0.3}\text{CoO}_3$, *J. Appl. Phys.* **111**, 063722 (2012).

- [27] Y. Y. Zhao, H. W. Yang, Y. Liu, H. Kuang, M. Zhang, W. L. Zuo, J. Wang, F. X. Hu, J. R. Sun, and B. G. Shen, Strain-induced high coercivity in $\text{La}_{0.7}\text{Sr}_{0.3}\text{CoO}_3$ films, *IEEE Trans. Magn.* **51**, 2100804 (2015).
- [28] B. Li, R. V. Chopdekar, A. M. Kane, K. Hoke, A. T. N'Diaye, E. Arenholz, and Y. Takamura, Thickness-dependent magnetic and electrical transport properties of epitaxial $\text{La}_{0.7}\text{Sr}_{0.3}\text{CoO}_3$ films, *AIP Adv.* **7**, 045003 (2017).
- [29] I. Pallecchi, F. Cagliaris, and M. Putti, Thermoelectric properties of iron-based superconductors and parent compounds, *Supercond. Sci. Technol.* **29**, 073002 (2016).
- [30] B. Flebus, R. A. Duine, and Y. Tserkovnyak, Landau-Lifshitz theory of the magnon-drag thermopower, *Europhys. Lett.* **115**, 57004 (2016).
- [31] G. J. Snyder, R. Hiskes, S. DiCarolis, M. R. Beasley, and T. H. Geballe, Intrinsic electrical transport and magnetic properties of $\text{La}_{0.67}\text{Ca}_{0.33}\text{MnO}_3$ and $\text{La}_{0.67}\text{Sr}_{0.33}\text{MnO}_3$ MOCVD thin films and bulk material, *Phys. Rev. B* **53**, 14434 (1996).
- [32] M. Cutler and N. F. Mott, Observation of Anderson localization in an electron gas, *Phys. Rev.* **181**, 1336 (1969).
- [33] See Supplemental Material at <http://link.aps.org/supplemental/10.1103/PhysRevMaterials.5.035401> for a detailed comparison and analysis of hysteresis curves for the Nernst effect and magnetization.
- [34] Y. Pu, D. Chiba, F. Matsukura, H. Ohno, and J. Shi, Mott Relation for Anomalous Hall and Nernst Effects in $\text{Ga}_{1-x}\text{Mn}_x\text{As}$ Ferromagnetic Semiconductors, *Phys. Rev. Lett.* **101**, 117208 (2008).
- [35] R. Ramos, M. H. Aguirre, A. Anad3n, J. Blasco, I. Lucas, K. Uchida, P. A. Algarabel, L. Morell3n, E. Saitoh, and M. R. Ibarra, Anomalous Nernst effect of Fe_3O_4 single crystal, *Phys. Rev. B* **90**, 054422 (2014).
- [36] L. Onsager, Reciprocal relations in irreversible processes I, *Phys. Rev.* **37**, 405 (1931); Reciprocal Relations in Irreversible Processes II, **38**, 2265 (1931); H. B. Callen, The application of Onsager's reciprocal relations to thermoelectric, thermomagnetic, and galvanomagnetic effects, *ibid.* **73**, 1349 (1948).
- [37] N. F. Mott and H. Jones, *The Theory of the Properties of Metals and Alloys* (Dover, New York, 1958).
- [38] N. Nagaosa, J. Sinova, S. Onoda, A. H. MacDonald, and N. P. Ong, Anomalous Hall effect, *Rev. Mod. Phys.* **82**, 1539 (2010).
- [39] R. Karplus and J. M. Luttinger, Hall effect in ferromagnetics, *Phys. Rev.* **95**, 1154 (1954).
- [40] M. V. Berry, Quantal phase factors accompanying adiabatic changes, *Proc. R. Soc. London* **392**, 45 (1984).
- [41] M. Onoda and N. Nagaosa, Topological nature of anomalous Hall effect in ferromagnets, *J. Phys. Soc. Jpn.* **71**, 19 (2002).
- [42] J. Smit, The spontaneous Hall effect in ferromagnetics I, *Physica* **21**, 877 (1955); The spontaneous Hall effect in ferromagnetics II, **24**, 39 (1958).
- [43] L. Berger, Side-jump mechanism for the Hall effect of ferromagnets, *Phys. Rev. B* **2**, 4559 (1970).
- [44] S. Onoda, N. Sugimoto, and N. Nagaosa, Intrinsic Versus Extrinsic Anomalous Hall Effect in Ferromagnets, *Phys. Rev. Lett.* **97**, 126602 (2006).
- [45] D. Xiao, Y. Yao, Z. Fang, and Q. Niu, Berry-Phase Effect in Anomalous Thermoelectric Transport, *Phys. Rev. Lett.* **97**, 026603 (2006).
- [46] A. Ghosh, R. Das, and R. Mahendiran, Skew scattering dominated anomalous Nernst effect in $\text{La}_{1-x}\text{Na}_x\text{MnO}_3$, *J. Appl. Phys.* **125**, 153902 (2019).
- [47] <http://mgml.eu>.